

Contents lists available at ScienceDirect

Petroleum Science

journal homepage: www.keaipublishing.com/en/journals/petroleum-science



Original Paper

High-temperature resistant polymer nanocomposites with exfoliated organic-modified montmorillonite nanosheets strongly adsorbed on polymer chains



Dong-Yin Wang, Chang-Feng Chen, Fei Ju, Yang-Chuan Ke *

China National Petroleum Cooperation Key Laboratory of Nano-Chemistry, College of Science, China University of Petroleum, Beijing, 102249, China

ARTICLE INFO

Article history: Received 27 January 2024 Received in revised form 1 July 2024 Accepted 2 July 2024 Available online 2 July 2024

Edited by Min Li

Keywords:
Adsorption chain
Exfoliated montmorillonite nanosheet
In situ polymerization
Water-soluble
High-temperature resistance

ABSTRACT

It has been demonstrated that almost all polymer-clay nanocomposites show higher temperature stability than that of pure polymer, which is attributed to the active exfoliated clay nanosheet firmly adsorbed onto the polymer chains, due to polerization and nucleation effect, the clay nanosheets could protect the polymer chains from destroying. To prove such mechanism, the water-soluble polymer nanocomposites (AAA/SLS-MMT) were synthesized by the in-situ polymerization of 2-acrylamide-2methyl-propane sulfonic acid, acrylamide, 4-acryloylmorpholine, and organically modified montmorillonite. The techniques of nuclear magnetic resonance, atomic force microscopy and scanning electron microscopy etc., clearly characterized the successful synthesized of sample's structure, the exfoliated MMT nanosheet adsorbed polymer chain's scale, and well-dispersed morphology, espectively. The adsorption model, X-ray photoelectron spectroscopy presented the existence of strong adsorption, while molecular simulation calculations first concluded that the strong adsorption energy was -13032.06 kcal/ mol. Thermo-gravimetric-analysis proved the temperature of maximum thermal degradation of powder sample (AAA/1.0 wt% SLS-MMT) was over 298 °C. After ageing at 180 °C for 4 h, the apparent viscosity of 5 g/L AAA/1.0 wt% SLS-MMT aqueous solution was 326.7 mPa·s, while that of pure polymer (AAA) was only 8.3 mPa·s. This optimized sample has the smallest FLAPI value at all test temperatures from 180 to 220 °C in both fresh and salt water based drilling fluid. All the evidences of high temperature resistance indicate that the strong adsorption can enhance the thickness of hydrated shell and adsorption of clay particles in drilling fluid at high temperature. Such mechanism supplied the better way to design hightemperature resistant fluid loss additives for deep and ultra-deep oil and gas formation engineering. © 2024 The Authors. Publishing services by Elsevier B.V. on behalf of KeAi Communications Co. Ltd. This is an open access article under the CC BY license (http://creativecommons.org/licenses/by/4.0/).

1. Introduction

Currently, shallow gas and oil fields are gradually depleted, the depth of exploration is increasing, and the temperature of the bottom hole also goes up (Abdo and Haneef, 2013; Sepehri et al., 2018; Liu et al., 2020). Developing high-temperature resistant water-based drilling fluids (WBDFs) is necessary to meet the drilling specifications for ultra-deep and deep wells (Aghdam et al., 2020). The "blood" of drilling operations is drilling fluid. It can avoid deposition, stabilize the borehole, maintain fluid loss control, lubricate the drill pipe, and stop wall collapse (Baba Hamed and Belhadri, 2009; Akpan et al., 2019; Mohamed et al., 2021). The superior filtration and rheology characteristics of WBDFs are crucial

to decreasing the operating time and increasing the efficacy of the drilling process. Nevertheless, at high temperatures, the rheological characteristics of WBDFs degrade, leading to wellbore leakage, wall collapse, stuck drilling tools, and other accidents (Epelle and Gerogiorgis, 2019). It is imperative to develop WBDF additives that are resistant to high temperatures and have exceptional rheological characteristics and filtering capabilities at elevated temperatures (Akhtarmanesh et al., 2013). Copolymer nanocomposites are employed as additives for WBDFs and have shown excellent high-temperature resistance during ultra-deep and deep well drilling operations (Hafshejani et al., 2016; Moslemizadeh et al., 2017; Ma et al., 2018; Hao, 2019; Li et al., 2023). To facilitate frequent ultra-deep and deep well drilling operations, the superior filtration loss performance and rheological characteristics of the WBDFs can be maintained at high temperatures (Wang et al., 2012; Yang et al., 2017b).

E-mail addresses: key@cup.edu.cn, kyc099@sohu.com (Y.-C. Ke).

^{*} Corresponding author.

Montmorillonite (MMT) is a two-dimensional layered silicate known as a 'universal material' (Zhao et al., 2020; Huang et al., 2021; Peng et al., 2021), which offers abundant availability, minimal cost, and a distinctive electronegativity (Dziadkowiec et al., 2017; Chen et al., 2020). MMT layers with strong cation exchangeability can be developed into hydrophilic nanocomposites (Ke, 2009; Yu et al., 2019; Xie et al., 2020; Quainoo et al., 2021). Recently, there has been a growing utilization of MMT-based nanocomposites as materials for WBDFs (Weng et al., 2016; Slaný et al., 2019).

Exfoliated MMT nanosheets possess a substantial length-to-diameter ratio, significant specific surface area, and excellent adsorption properties and chemical reactivity. Nanocomposites with exfoliated MMT sheets have better high-temperature resistance and nano-barrier and mechanical properties than pure polymer (Chin et al., 2001; Zhu et al., 2019; Fekry et al., 2020; Abdel Karim et al., 2021; Zhao et al., 2022). The exfoliated MMT nanosheets in nanocomposites can effectively adsorb on the polymer surface, thereby enhancing the mechanical strength of the nanocomposite and functioning as a nano-barrier to protect the polymer chain from degradation at high temperatures (Chiou et al., 2014; Osman et al., 2015; Ejder Korucu et al., 2016; Yang et al., 2017a; Alani et al., 2020).

To date, exfoliated MMT nanosheets have been prepared by physical or chemical methods (Luckham and Rossi, 1999; Ma and Sasaki, 2010; Coleman et al., 2011; Huang et al., 2016). The main physical methods include grinding, ultrasonication, freeze-drying, and their combinations (Chaudhary and Liu, 2013; Galimberti et al., 2014; Chen et al., 2019). Melt, solution, and in situ polymerization exfoliation are examples of chemical exfoliating techniques. In situ polymerization exfoliation is the most used method and has been extensively studied (Roghani Mamaqani et al., 2011; Gunning et al., 2014; Zhang et al., 2015; Wang et al., 2023). For example, Hu and Ke (2019) prepared a high-temperature resistant polymer nanocomposite oil repellent with a single sheet of MMT nanosheets using in situ polymerization. Similarly, Xing et al. (2019) synthesized a high-temperature WBDF nanocomposite as a drag reducer with an exfoliated MMT nanosheet. Wang et al. (2022a) developed a fluid loss reducer by incorporating exfoliated MMT nanosheets into a polymer nanocomposite. In a typical process of in situ polymerization, a surfactant solution is first added to an MMT suspension to expand the spacing between the MMT interlayers. Next, the monomer enters the MMT interlayer and undergoes a polymerization reaction (Briesenick and Bremser, 2015; Hojiyev et al., 2017). Finally, an organic-modified MMT nanosheet is uniformly dispersed in a polymer matrix.

When exposed to high temperatures, the natural polymers in WBDFs undergo rapid degradation, causing a significant decrease in their apparent viscosity (AV). This lead to poor filtration performance. To solve this problem, various synthetic polymers, such as polyacrylonitrile, polyacrylamide, and polyacrylic acid (Yu, 2015; Saboori et al., 2019; Xing et al., 2020), have been introduced as additives. However, these traditional homopolymers have poor resistance to temperature, salt, and shear. Hence, the copolymerization of various functional monomers is a promising approach to producing polymers resistant to high temperatures (Huo et al., 2018; Luo et al., 2018). Drilling fluids can effectively be thickened with acrylamide (AM), a water-soluble substance, owing to its ability to hydrogen bond with NH₂ groups. Because 2-acrylamido-2-methyl-1-propanesulfonic acid (AMPS) has a sulfonic acid group, it has a high thermal resistance. The six-ring rigid structure of 4acryloylmorpholine (ACMO) renders it exceptionally stable when exposed to high temperatures.

In this study, AM, AMPS, ACMO, and sodium 1-dodecanesulfonate (SLS)-intercalated MMT (SLS-MMT) was

prepared the water-soluble copolymerized nanocomposite (AAA/ SLS-MMT). The adsorption energies among the polymer chains and the nanosheets of exfoliated silicate were calculated. Furthermore, the efficacy of the nanocomposites at elevated temperatures in deionized water (DI) and drilling fluids was evaluated. Finally, the filtrate volume of American Petroleum Institute (API) standard conditions ($FL_{\rm API}$) was measured, and the stability of the nanocomposite at elevated temperatures was investigated. The results indicate that AAA/SLS-MMT has the potential to reduce fluid loss in WBDFs for ultra-deep and deep wells.

2. Material and methods

2.1. Materials

Na-MMT (one mol/kg of cation exchange capacity) was produced by Huaian Saibei Technology Co., Ltd. (Zhangjiakou, China). 1-Dodecanesulfonic acid sodium salt (SLS, 98%) and acrylamide (AM, 98%) were purchased from Tianjin Guangfu Fine Chemical Research Institute (Tianjin, China). 2-Acrylamide-2-methyl-propane sulfonic acid (AMPS, 99%) and 4-acryloylmorpholine (ACMO, 98%) were acquired from Aladdin Biochemical Co., Ltd. (Shanghai, China). Triallyl isocyanurate (TAIC, 98%) was provided by Shanghai Macklin Biochemical Co., Ltd. (Shanghai, China). Ammonium persulfate ((NH₄)₂S₂O₈, 98%), sodium hydroxide (NaOH, 96%), absolute ethanol (CH₃CH₂OH, 99.7%), and sodium bisulfite (NaHSO₃, 98%) were obtained from Tianjin Fuchen Fine Chemical Research Institute (Tianjin, China).

2.2. Methods

2.2.1. Synthesis of nano-intermediates

SLS-MMT was synthesized using a previously reported method (Wang et al., 2022a). Na-MMT (10.00 g) was put in a flask containing DI water (150 mL). The flask was then allowed to heat at 30 °C and agitated mechanically for 30 min. Then, the pH of the mixture was adjust to 1 by HCl. After bringing it to 80 °C, it was agitated for 30 min. The resultant mixture was subsequently continuously stirred for 12 h, while the SLS solution (3.27 g) was incorporated dropwise into the aforementioned mixture. The sample was then obtained by centrifugation, and it was washed until the supernatant fluid's pH was almost 7. Finally, the product (SLS-MMT) was vacuum dried at 70 °C for 24 h. The sample was crushed and sieved with the help of a 200 mesh screen. The preparation procedure is illustrated in Fig. 1.

2.2.2. Preparation of nanocomposites

To fabricate AAA/SLS-MMT nanocomposites, in situ free radical polymerization was implemented. After dispersing the aforementioned SLS-MMT in DI water (75 mL) using ultrasound for 10 min, the resulting mixture was agitated at 25 °C for 30 min. After that, AM (12.25 g), AMPS (7.50 g), and ACMO (5.25 g) were added to the three-necked flask. After that, the mixture was agitated for 30 min in a nitrogen environment after the pH had been adjusted to 6. Subsequently, NaHSO₃ and $(NH_4)_2S_2O_8$ (0.3 wt%, molar ratio:1:1) was added as initiator. After a 6 h reaction, the temperature was finally raised to 50 °C. The product was rinsed to eliminate excess initiators and monomers. Then, the obtained samples were crushed and dried for 24 h at 70 °C. The final sample was ground and sieved with 200 mesh. Based on the amount of SLS-MMT (0.25 or 0.50 g), the samples are denoted as AAA/1.0 wt% SLS-MMT and AAA/2.0 wt% SLS-MMT, respectively. The AAA was synthesized without adding SLS-MMT. The synthesis process is exhibited in Fig. 2.

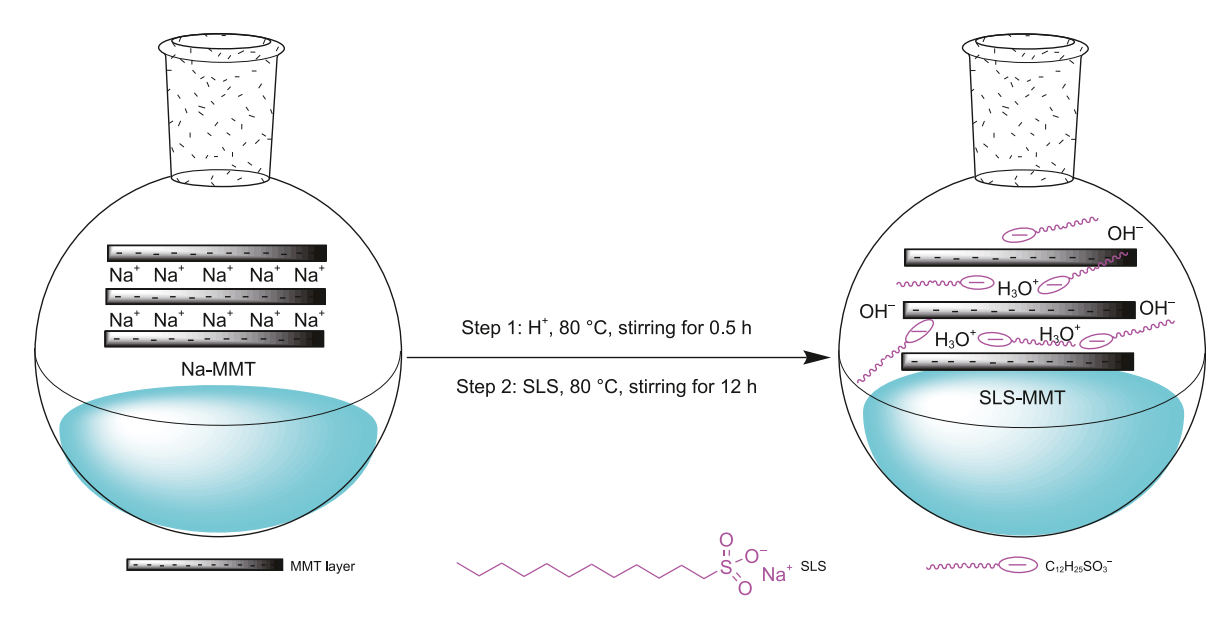


Fig. 1. Schematic of the preparation of SLS-MMT.

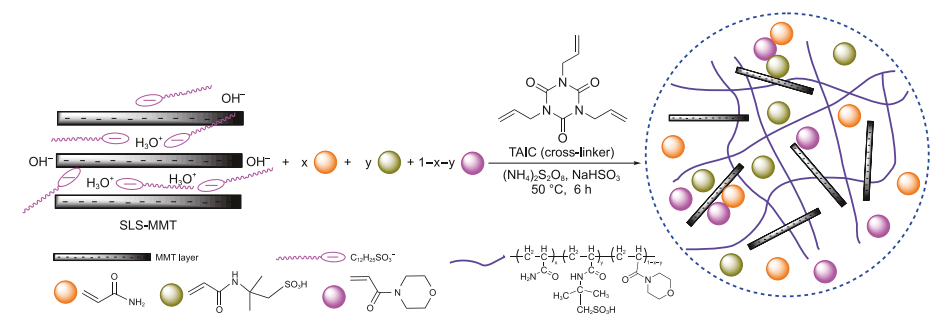


Fig. 2. Schematic illustrating the fabrication process of AAA/SLS-MMT nanocomposites.

2.3. Characterisation

The Bruker D8 Advance, equipped with a nickel-filtered Cu-Kα radiation source ($\lambda = 0.1540$ nm), was utilized to obtain X-ray diffraction (XRD) patterns of the materials. FT-IR spectra (4000–400 cm⁻¹) were recorded using a PerkinElmer Spectrum GX spectrophotometer (Waltham, MA, USA). The ¹H-nuclear magnetic resonance (NMR) spectroscopy (Bruker, Avance, 400 MHz, Billerica, MA, USA) of AAA was tested. Thermogravimetric analysis (TGA; Netzch STA409PC, Selb, Germany) was used to record the weight losses of samples. The morphologies of polymer nanocomposites and filter cakes were examined by scanning electron microscopy (SU8010, Hitachi, Tokyo, Japan). Transmission electron microscopy (TEM; FEI Tecnai F20; Hillsboro, OR, USA) images were obtained with a 200 kV accelerating voltage. VG-ESCALAB250Xi, a Thermo Fisher Scientific device calibrated with the C 1s peak at 284.6 eV, was employed to conduct X-ray photoelectron spectroscopy (XPS). Detailed surface information on the polymer nanocomposites was determined through atomic force microscopy (AFM; Keysight 5500, Agilent, USA).

From the XRD patterns, the distance between the silicate layers could be calculated by the Bragg's law:

$$2d\sin\theta = n\lambda \tag{1}$$

where n, λ , d, 2θ represent the reflection order (n = 1), wavelength of the X-ray, diffraction interplanar distance (nm) and diffraction

angle (°), respectively.

2.4. Rheology measurements

The viscometer, Brookfield DV-II + Pro (Rotor speed: 60 rpm; Middleboro, MA, USA), was applied to measure the apparent viscosity. AV measurements were performed at various ageing temperatures and ageing times using aqueous solutions (5 g/L).

The AV of water-based drilling fluid system was tested by six-speed rotational viscometer (MOD.ZNN-D6, Qingdao Haitongda Special Instrument Co., Ltd., Qingdao, China). The values at 600 (θ_{600}) were employed to calculate the AV, using Eq. (2) according to the API standard, and the units of AV was mPa·s.

$$AV = \theta_{600}/2 \tag{2}$$

2.5. Fluid loss in simulated drilling fluid

 Na_2CO_3 (3.5 wt% Na-MMT-based), Na-MMT (4.0 wt% DI waterbased), and AAA/1.0 wt% SLS-MMT (0 or 0.5 wt%) were added to DI water (400 mL) to prepare a simulated drilling fluid based on fresh water. After that, the mixture was being agitated continuously for 20 min at 10,000 rpm, then kept at 25 °C for 24 h.

The system of saturated brine drilling fluid was produced by adding NaCl (37.0 wt%) to the fresh water-based simulated drilling

fluid described above. To make the composite brine drilling fluid, $CaCl_2$ (2.60 g), $MgCl_2$ (6.90 g), and NaCl (16.00 g) were dissolved in the same fluid.

The high temperatures and pressure filtering device (MOD.GGS42-2A, Qingdao, China: Shande Petroleum Instrument Co., Ltd.) was utilized to measure the volume of filtrate (*FL*_{API}).

2.6. Measurements of zeta potential

A simulated drilling fluid system's stability was evaluated by utilizing a zeta potential analyzer (Malvern Zetasizer Nano ZS ZEN3600, (Malvern, UK)/Malvern Instruments Ltd.). The 100-fold dilution of the colloid of simulated drilling fluid was performed prior to the measurements.

2.7. Calculation of adsorption energy

The strong adsorption between the polymer and the exfoliated MMT nanosheet was verified using Materials Studio molecular simulation software. An amorphous Cell and Forcite were used for the model construction, geometric optimization, molecular dynamics balance, and mechanical property evaluation of the exfoliated MMT-polymer nanocomposite. Firstly, a monoclinic cell (C2/ m) of symmetry type (L2PC) was built, and the lattice constant $(a \times b \times c)$ was 5.23 \times 9.06 \times 12.50 Å. Secondly, the spatial coordinates and charge amount of atoms were added (Li et al., 2016). Thirdly, the supercell $(4a \times 2b \times 1c)$ was established by symmetry. Finally, according to the principle of substitution, the crystal model of MMT was obtained, and the initial lattice parameters was a = 20.92 Å, b = 18.12 Å, c = 12.50 Å, $\alpha = \gamma = 90^{\circ}$, $\beta = 99^{\circ}$. Due to the universal force field (UFF) was a pure diagonal harmonic force field, and suitable for almost all elements of the periodic table. So, the UFF was used and the number of polymer chains was set as 4. The mole ratio between monomers (AM:AMPS:ACMO) was the ratio used in the experiment (5:2:3). The total energy of the exfoliated MMT nanosheet and the polymer chain (E_{total}), the energy of the exfoliated MMT nanosheet (E_{e-MMT}), and the energy of the polymer chain $(E_{polymer})$ were calculated. The adsorption energy between the MMT and polymer chains (ΔE_{int}) was calculated by Eq. (3).

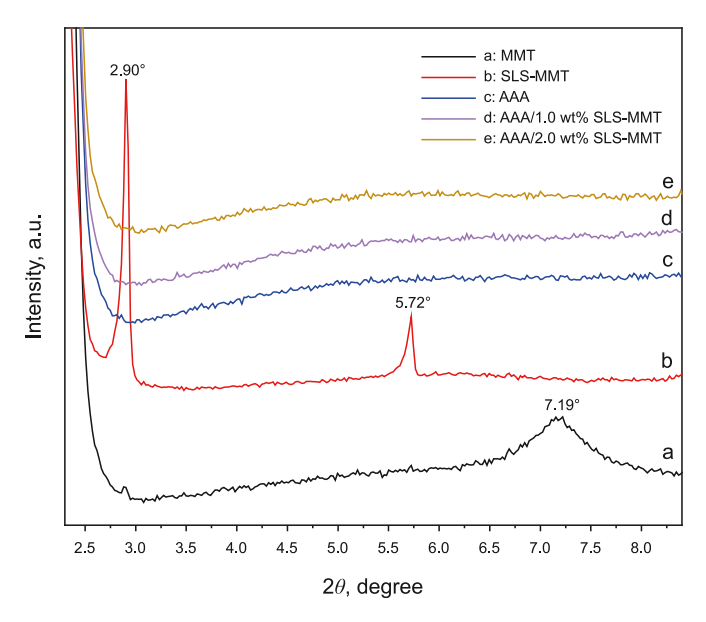


Fig. 3. XRD patterns of a: MMT; b: SLS-MMT; c: AAA; d: AAA/1.0 wt% SLS-MMT and e: AAA/2.0 wt% SLS-MMT.

$$\Delta E_{\rm int} = E_{\rm total} - E_{\rm polymer} - E_{\rm e-MMT} \tag{3}$$

3. Results and discussion

3.1. XRD

XRD was employed to examine the lamellar gap between the silicate layers. Fig. 3 presents the XRD patterns of MMT, SLS-MMT, AAA, AAA/1.0 wt% SLS-MMT, and AAA/2.0 wt% SLS-MMT. The diffraction pattern of MMT (Fig. 3(a)) has a characteristic diffraction peak (7.19°), this corresponds to 1.23 nm d-spacing. The peaks of SLS-MMT exhibit at 2.90° and 5.72° (Fig. 3(b)), which correspond to the d-spacing of 3.04 and 1.54 nm, respectively. The increased interlayer distance compared to that in pure MMT indicates that SLS-MMT was successfully prepared using SLS treatment. However, the AAA/SLS-MMT nanocomposites did not observe diffraction peaks (Fig. 3(d)—(e)). Owing to the heat of polymerization further expands the interlayer spacing of SLS-MMT, facilitating their uniform distribution in the polymer matrix. The formation of polymer nanocomposites and SLS-MMT was successfully verified by the XRD data.

3.2. FT-IR

The chemical composition as well as molecular structure of the samples were examined using FT-IR spectroscopy. In the MMT layers, the stretching vibration of O–H belonging to Si–OH and Al–OH is linked to the absorption peak at 3611 cm⁻¹ in Fig. 4(a). The hydroxyl stretching vibration absorption peak of free water in MMT is at 3423 cm⁻¹. The sharp peak at 1630 cm⁻¹ in MMT ascribes to the bending vibrations of interlayer water molecules H–O–H. The distinctive peaks at 1040, 524, and 471 cm⁻¹ are ascribed to stretching vibrations Si–O–Si. Si–O–Al stretching vibration is correlated with the peak at 795 cm⁻¹. The SLS-MMT FT-IR spectrum (Fig. 4(b)) exhibits two prominent peaks at 2848 and 2918 cm⁻¹, which correspond to both the asymmetric and symmetric SLS –CH₂ telescopic vibrations, respectively. The peak at 1676 cm⁻¹ of AAA corresponds to the C=O group in AM, as illustrated in Fig. 4(c). For

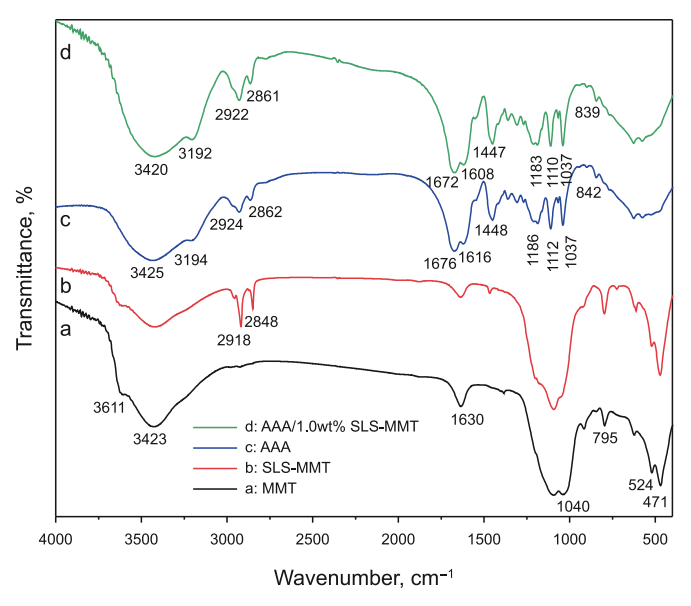


Fig. 4. FT-IR spectrum of a: MMT; b: SLS-MMT; c: AAA and d: AAA/1.0 wt% SLS-MMT.

the CONH₂ group belonging to AM, the N-H stretching vibration was detected at 3194 cm⁻¹. The peaks observed at 2924 and 2862 cm⁻¹ corresponded to the CH₂ stretching vibrations (asymmetric and symmetric) in AM. Furthermore, the sulfonic acid group peak was detected at around 1186 cm⁻¹, whereas the distinctive peak at 1112 cm⁻¹ represents S=O's asymmetric stretching vibration in SO_3^{2-} . These findings support the existence of the AMPS structure in AAA. Furthermore, a six-membered ring structure is characterized by a peak at 1616 cm⁻¹ while the peak at 1447 cm⁻¹ represents the six-membered ring's stretching vibration of C-N, while the fingerprint region's peak at 1037 cm⁻¹ represents the C-O group in the same ring. These peaks confirm the ACMO in AAA. As the content of SLS-MMT is very low, the exfoliated silicate nanosheets will be of very sparse distribution, so the peaks of Si-O-Si bond's bending vibrations in the spectra of AAA/1.0 wt% SLS-MMT sample may be weak of covered (Fig. 4(d)). In short, the FT-IR findings support the successful preparation of SLS-MMT, AAA, and AAA/1.0 wt% SLS-MMT (Liu et al., 2018; Tian et al., 2019).

3.3. ¹H-NMR analysis

¹H-NMR is used to determine the molecular structure based on the chemical shift of hydrogen in the molecule. The prominent signal at 4.69 ppm in Fig. 5 illustrates the residual protons in D₂O. The main chain protons of CH₂ are represented by the distinctive peak at 1.91 ppm (1). The single peak at 2.40 ppm (2) is ascribed to the CH proton present in the main chain. The double peak of 3.60, 3.47 ppm (8,9) represents the protons on the six-membered ring of ACMO. In addition, the broad peaks at 4.78, 4.53 ppm (4,3) represent the NH and NH2 protons in AMPS and AM, respectively. The shoulder peak at 2.99 ppm (6) corresponds to the proton of the CH₂ group in the AMPS side chain. The characteristic peak at 1.27-1.15 ppm (5) represents the protons of CH₃ in AMPS. Maybe, the active hydrogen proton (7) of SO₃H in AMPS is not present. Owing to the active hydrogen proton (7) occurs proton-exchange reaction with D₂O. In conclusion, the ¹H-NMR results confirm the successful synthesis of AAA.

3.4. SEM-EDS analysis

The elemental composition was ascertained by EDS, while SEM revealed the surface shape of the polymer nanocomposite. The SEM images as well as EDS analysis of AAA and AAA/1.0 wt% SLS-MMT are presented in Fig. 6. In Fig. 6(a), the macromolecular chain of

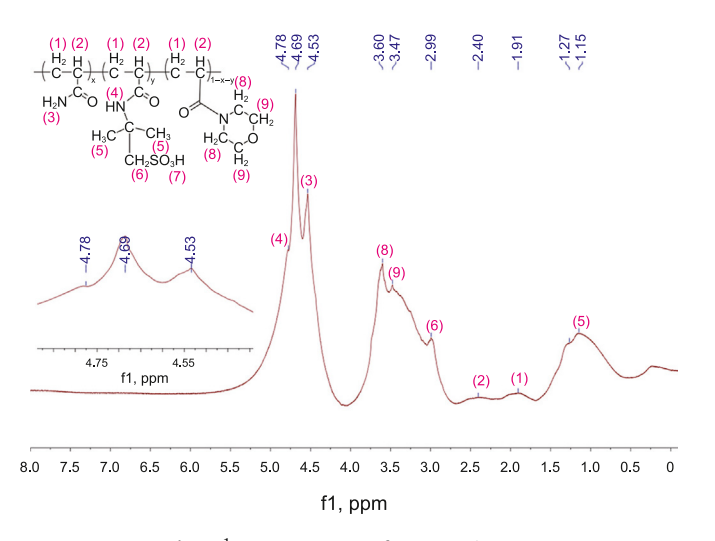


Fig. 5. 1 H-NMR spectrum of pure AAA in $D_{2}O$.

AAA is very thin and fragile, and the surface is smooth. From Fig. 6(b)—(c)) show the results of AAA/1.0 wt% SLS-MMT. Compared to AAA, the molecular chains of the nanocomposite are thicker and tougher and the porosity of the network structure is lower. Moreover, AAA/1.0 wt% SLS-MMT had a substantially rougher surface than AAA. Because of the adsorption of many SLS-MMT nanosheets on the surface of the polymer chain (Fig. 6(d)). The strongly adsorbed SLS-MMT can function as thermally insulating and saltresistant nanobarriers to prevent the rapid degradation of the polymer. Si, Na, Al, and Mg were found in the MMT nanosheets, while O, C, N, and S were confirmed to be present in the polymer by EDS analysis of AAA/1.0 wt% SLS-MMT (Fig. 6(d)—(e) and Table 1). The aforementioned findings collectively demonstrate the strong adsorption of SLS-MMT nanosheets onto the chains of the polymer.

3.5. TEM analysis

The dispersion of exfoliated SLS-MMT nanosheets within the polymer matrix was observed using TEM. The TEM images and EDS maps are shown in Fig. 7. The exfoliated organic-modified MMT nanosheets are observed in the polymer matrix (Fig. 7(a)). In the magnified images (Fig. 7(b)—(c)), many black lines (indicated by red arrows) corresponding to the exfoliated nanosheets are observed, providing evidence that the SLS-MMT nanosheets are substantially adsorbed on the polymer chains' surface and are uniformly distributed throughout the polymer matrix. In addition, the EDS maps (Fig. 7(d)) show N, S, C, and O in the polymer and Al, Mg, Si, and Na in the nanosheets. This finding provides further evidence that the exfoliated SLS-MMT nanosheets strongly adsorb to the polymer's surface. The exfoliated and well-dispersed SLS-MMT nanosheets are expected to improve the polymer nanocomposites' resistance to high temperatures.

3.6. TGA

The thermal degradation behaviour of AAA and AAA/SLS-MMT, studied by TGA, is shown in Fig. 8. The thermal degradation of AAA and AAA/SLS-MMT occurs in five stages. Due to the thermal decomposition of certain volatile components and free water, initial-stage weight loss occurs in stage one (below 125 °C). The minor reductions in weight during the second stage (125–250 °C) of AAA and AAA/SLS-MMT can be ascribed to the thermal degradation of bonded water in the samples. As the temperature increases, the third stage (250-330 °C) weight losses of AAA and AAA/SLS-MMT increase because of the thermal decomposition of the carbonyl (-C=O) and acylamino (-CONH₂) groups on the side chains of the polymer. The temperatures corresponding to the maximum thermal decomposition rate of AAA, AAA/1.0 wt% SLS-MMT, and AAA/2.0 wt% SLS-MMT are 275, 298, and 280 °C, respectively. The higher thermal decomposition temperature of AAA/1.0 wt% SLS-MMT suggests that the exfoliated SLS-MMT nanosheets on the surface can block the thermal degradation of the polymer chains. In the fourth stage, the weight losses of AAA and AAA/SLS-MMT are significant owing to the sulfonic acid group's (-SO₃H) thermal degradation, six-membered ring of sodium dodecyl sulfonate, and polymer side chains. The minimal weight loss observed during the fifth stage can be attributed to the thermal degradation of the primary polymerization chain (-C-C-). In summary, the exfoliated SLS-MMT nanosheets with strong adsorbed surfaces enhance the polymer's tolerance to elevated temperatures.

3.7. XPS

XPS provides information on the molecular structure, chemical

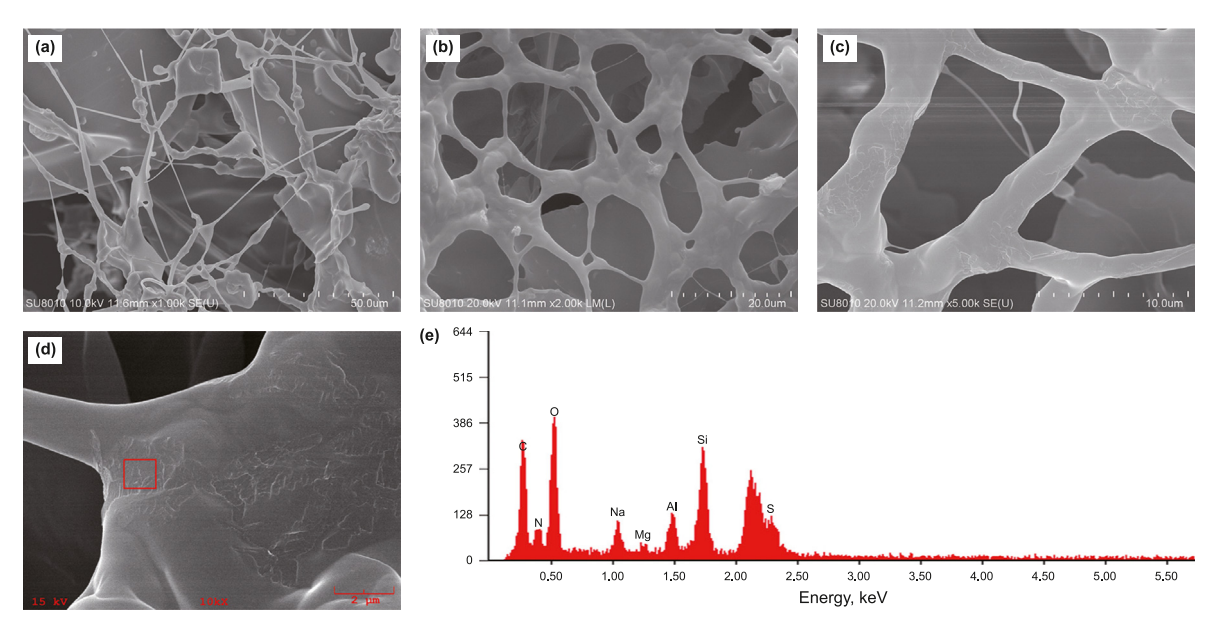


Fig. 6. SEM photographs of (a) AAA, (b)-(d) AAA/1.0 wt% SLS-MMT, and (e) EDS profile of AAA/1.0 wt% SLS-MMT.

Table 1 Energy dispersive spectrometer analysis of AAA/1.0 wt% SLS-MMT.

Element	С	N	0	S	Na	Mg	Al	Si
Content, wt%	41.00	11.10	30.45	3.62	2.76	0.57	2.92	7.57

bonds, elemental composition, and chemical state of a material. The survey spectra in Fig. 9(a) demonstrate that Al, O, and Si are present in MMT, while Al, O, C, Si, and S are present in SLS-MMT, indicating that SLS is successfully intercalated between MMT sheets. The existence of N, S, C, and O in AAA is also verified, while AAA/1.0 wt% SLS-MMT has additional Si, proving that the polymer

nanocomposite was successfully synthesized. The deconvoluted C 1s high-resolution spectrum of AAA is illustrated in Fig. 9(b). This spectrum reveals three distinct peaks at 286.29, 287.69, and 284.64 eV, which are the respective indications of N–C=O, C–O, and C–C groups. In comparison, the AAA/1.0 wt% SLS-MMT spectrum shows three distinct peaks at 284.49, 287.53, and 586.18 eV (Zhao et al., 2020). In Fig. 9(c), the N 1s high-resolution spectrum of AAA is deconvoluted into two characteristic peaks of 399.45 and 402.02 eV, which are attributed to NH/NH₂ and N–C=O groups, respectively, while the spectrum of AAA/1.0 wt% SLS-MMT shows two characteristic peaks at 399.28 and 401.93 eV (Bensalem et al., 2017). The O 1s peaks in the spectra of AAA and AAA/1.0 wt% SLS-MMT are located at 531.34 and 531.14 eV, respectively (Fig. 9(d)).

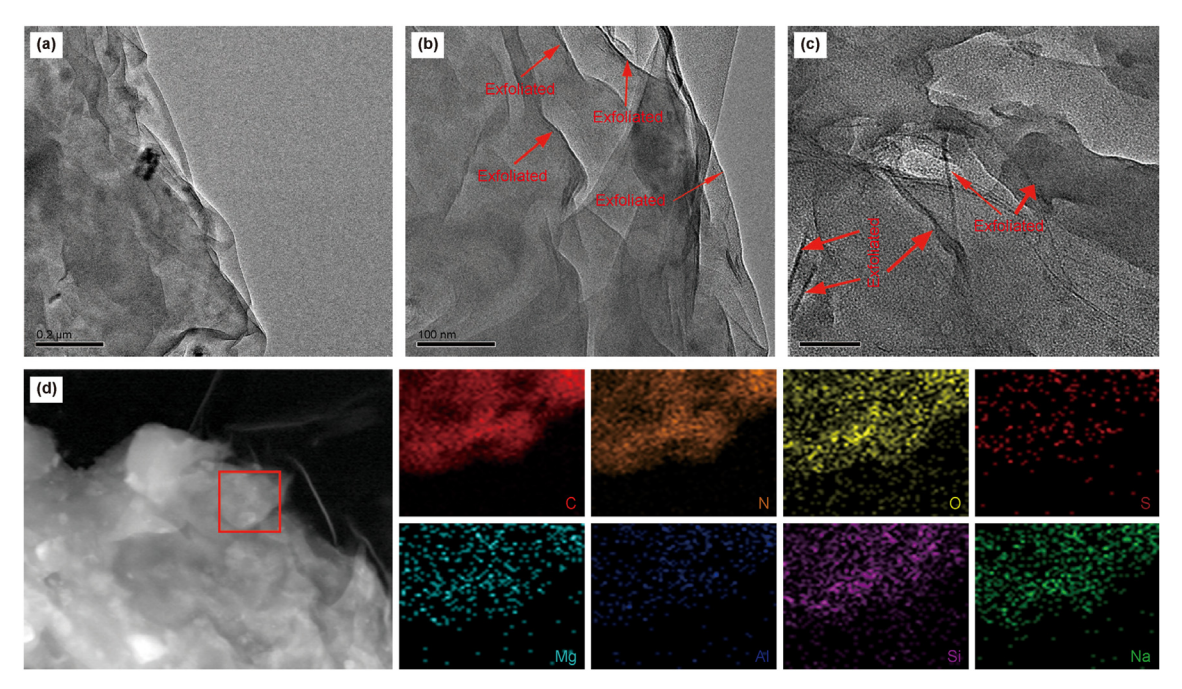


Fig. 7. (a)—(c) TEM images and (d) EDS analysis of AAA/1.0 wt% SLS-MMT. The red arrows indicate exfoliated MMT nanosheets.

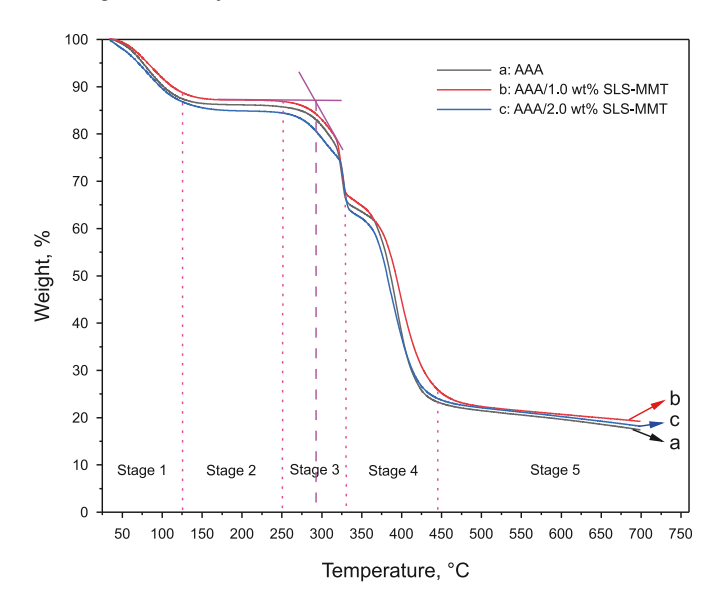


Fig. 8. TGA curves of a: AAA; b: AAA/1.0 wt% SLS-MMT and c: AAA/2.0 wt% SLS-MMT.

Two distinctive peaks in the AAA S 2p high-resolution spectrum are attributed to the $S_{\rm n}^{2-}$ and SO_x groups, respectively, at 161.91 and 167.95 eV; in contrast, the AAA/1.0 wt% SLS-MMT spectrum exhibits these same peaks at 161.90 and 167.76 eV (Fig. 9(e)) (Wang et al., 2022b). In conclusion, compared with AAA, the characteristic O 1s, S 2p, N 1s, and C 1s XPS peaks of AAA/1.0 wt% SLS-MMT shift to lower binding energies, possibly due to electron transfer from SLS-MMT to AAA in the nanocomposites. The XPS data further reveal strong adsorption between AAA and the exfoliated SLS-MMT nanosheets (Zhang et al., 2021), where adsorption may occur via hydrogen bonds, intermolecular forces, and van der Waals forces.

3.8. AFM analysis

The exfoliated SLS-MMT nanosheets were found to be substantially adsorbed to the polymer chain surface upon AFM examination of AAA and AAA/1.0 wt% SLS-MMT. Fig. 10(a)—(b) show the 3D morphology of AAA and AAA/1.0 wt% SLS-MMT, respectively. The surface of AAA is smooth, while many bumps are observed on the surface of AAA/1.0 wt% SLS-MMT due to the adsorption of the exfoliated SLS-MMT nanosheets. Fig. 10(c)—(d) show potential maps of AAA and AAA/1.0 wt% SLS-MMT, respectively. The average heights of AAA and AAA/1.0 wt% SLS-MMT are 17.85 nm and 21.13 nm, respectively, as calculated using analysis software. The observed height difference of 3.28 nm can be attributed to the exfoliated SLS-MMT nanosheets, providing further evidence of the strong adsorption of SLS-MMT nanosheets onto the chains of the polymer.

3.9. Characteristics of nanocomposites in aqueous solutions

3.9.1. Temperature and concentration dependence of AV

Fig. 11(a) reveals that the AV values increased with concentration, reaching a maximum at concentrations greater than 5 g/L, suggesting the fact that the adsorbed silicate nanosheets formed crosslinked networks. Among the investigated concentrations, AAA/1.0 wt% SLS-MMT exhibited the highest AV values, which is in agreement with the SEM findings and indicates that it is capable of forming the most effective crosslinked network structure. The AV values of the AAA and AAA/SLS-MMT solutions are displayed in Fig. 11(b), where it is observed that the AV values exhibit a decline

as the temperature rises from 25 to 95 °C. At 95 °C, the AV values of AAA, AAA/1.0 wt% SLS-MMT, and AAA/2.0 wt% SLS-MMT were 108.3, 150.0, and 141.7 mPa·s, respectively. The improved temperature resistance of AAA/1.0 wt% SLS-MMT was demonstrated by its consistently higher AV at all measured temperatures compared to the other samples. Exfoliated and uniformly dispersed SLS-MMT nanosheets function as nanobarriers, effectively impeding polymer degradation by adsorbing strongly onto the surfaces of the polymer chains. The results indicates that AAA/1.0 wt% SLS-MMT is a promising polymer nanocomposite of high temperature resistance.

3.9.2. Impact of ageing on AV of aqueous solution

The AV was examined at various ageing temperatures and times. Fig. 12(a) shows the relationship between the AV and ageing temperature at an ageing time of 4 h. The AV values of AAA and AAA/ 1.0 wt% SLS-MMT increase with increasing temperature. A polymer chain crosslinked at an appropriate temperature can increase the AV. At a temperature of 150 °C, the AV of AAA/1.0 wt% SLS-MMT reaches the maximum (1116.7 mPa·s). However, the highest AV of AAA (727.0 mPa·s) is achieved at 140 °C. Compared to AAA, the strongly adsorbed SLS-MMT nanosheets on AAA enhance the temperature resistance of AAA/1.0 wt% SLS-MMT by 10 °C. With increasing temperature, the movement of the polymer chains intensifies and more polymer chains can interact with the exfoliated MMT nanosheets to produce more nanobarriers and restrict the thermal degradation of the nanocomposite. However, with a further increase in temperature, the polymer chains are destroyed, and the viscosity of the aqueous solution decreases rapidly.

The *AV* values of different ageing times are presented in Fig. 12(b), and the ageing temperature is 160 °C. As the ageing time increased from 0 to 3 h, the *AV* of AAA/1.0 wt% SLS-MMT rose from 376.7 to 1053.0 mPa s. The maximum *AV* of AAA (813.3 mPa s) was observed at 2 h, after which it subsequently decreased. But, the *AV* of AAA/1.0 wt% SLS-MMT is still higher than that of AAA for ageing times of 3–8 h. AAA/1.0 wt% SLS-MMT exhibited an *AV* of 86.67 mPa s following 8 h of ageing. The AAA, however, measured only 6.67 mPa s. Despite undergoing an extended period of ageing (8 h) at 160 °C, the AAA/1.0 wt% SLS-MMT polymer chains remained resistant to destruction at elevated temperatures due to the protective effect of the MMT. AAA/1.0 wt% SLS-MMT is therefore a potentially effective additive for high-temperature WBDFs.

3.10. AV of aged WBDFs

Finally, the AV values of WBDFs containing 0.5 wt% AAA/1.0 wt% SLS-MMT were evaluated using a six-speed rotational viscometer after aging for 16 h at various temperatures. Fig. 13 shows that as the aging temperature increases (180–220 °C), the AV values of saturated brine and composite brine WBDF systems decreases rapidly, from 11 to 3 mPa·s and from 8 to 2 mPa·s, respectively. However, the corresponding decrease in the AV of the fresh water system was minimal (5 mPa·s). The good high-temperature performance in the freshwater system is attributed to the strongly adsorbed exfoliated SLS-MMT nanosheets on the surface of polymer chains. In contrast, Ca^{2+} and Mg^{2+} in the brine solutions degrade the hydration shell and electric double layer of the WBDFs, resulting in poor high-temperature resistance. The limited performance of the developed additive in brine solutions should be addressed in the future studies.

3.11. FL_{API} at high temperatures

3.11.1. AAA/1.0 wt% SLS-MMT in fresh WBDFs systems

The resistance of AAA and AAA/1.0 wt% SLS-MMT to high

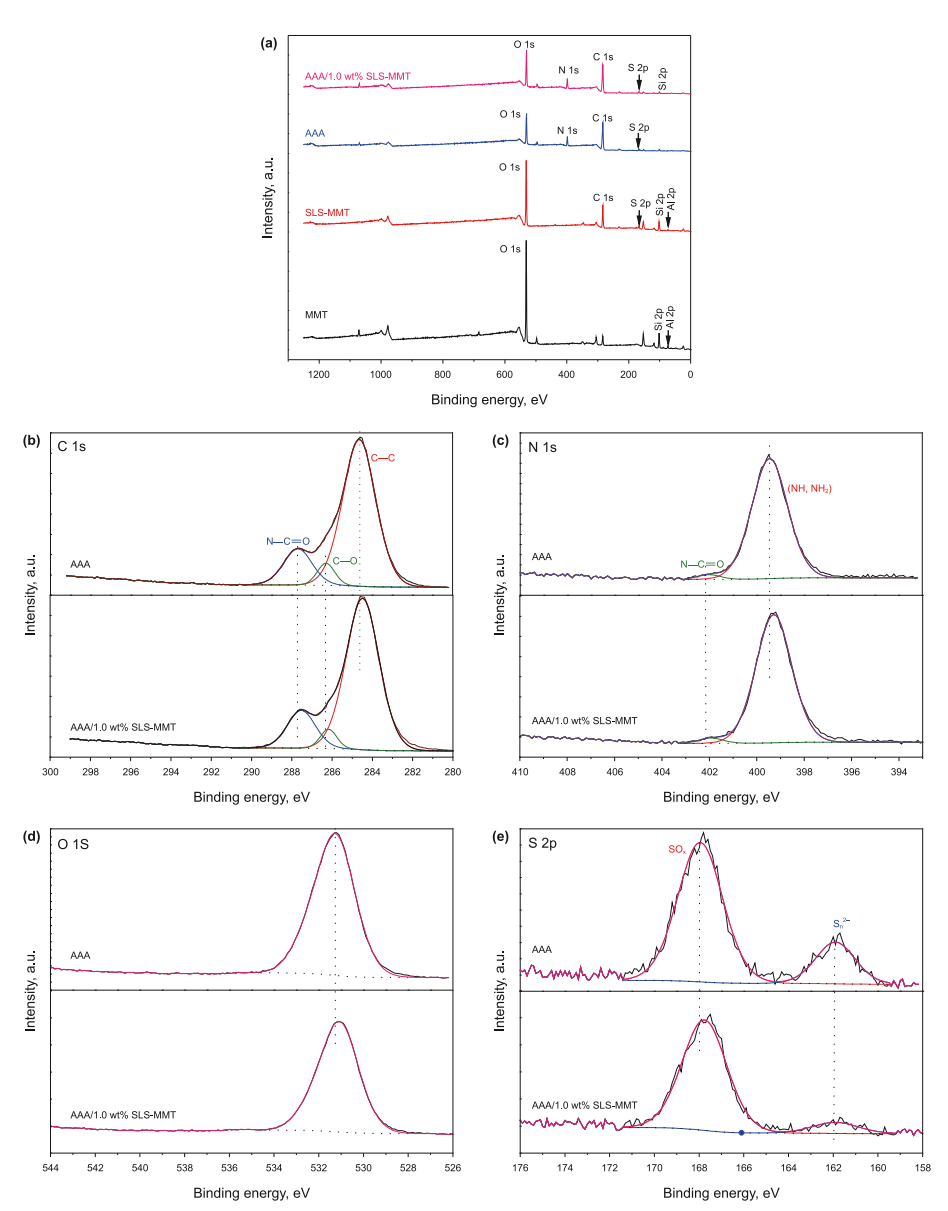


Fig. 9. (a) XPS survey spectra of MMT, SLS-MMT, AAA, AAA/1.0 wt% SLS-MMT, high-resolution spectra of AAA and AAA/1.0 wt% SLS-MMT at (b) C 1s, (c) N 1s, (d) O 1s and (e) S 2p core levels.

temperatures was assessed using fluid loss experiments conducted in accordance with API standard procedures. As illustrated in Fig. 14, FLAPI increases with increasing temperature from 180 to 220 °C. After adding the additives to a WBDFs system, FLAPI decreases significantly, where the system with AAA/1.0 wt% SLS-MMT has the smallest FL_{API} at all tested temperatures. The FL_{API} of the initial drilling fluid system at 220 °C was 40 mL. In contrast, systems containing 0.5 wt% AAA and 0.5 wt% AAA/1.0 wt% SLS-MMT had significantly lower FL_{API} values of 15.6 and 11.8 mL, respectively. While both additives reduce the filtration loss, the previously discussed functionality provided by MMT further improves the performance compared to the use of AAA alone. In addition to the thermal and structural stability provided by SLS-MMT, these nanosheets increase the molecular weight by increasing the number of polymer chains. In summary, AAA/1.0 wt% SLS-MMT can be employed as a high-temperature-resistant fluid loss additive in deep and ultra-deep reservoirs.

3.11.2. AAA/1.0 wt% SLS-MMT in brine-based drilling fluid systems

To investigate the salt resistance of the polymer nanocomposite, FL_{API} was measured in brine-based saturated and composite drilling fluid systems, and the results are shown in Fig. 15. The saturated brine system has a FLAPI of 170 mL at 180 °C. The high FLAPI value is because Na⁺ ions can break the hydration membrane and destroy the double electric layer, thereby causing the colloidal solution to agglomerate and lose its colloidal performance. After the addition of 0.5 wt% of AAA or AAA/1.0 wt% SLS-MMT to the saturated brine system, the FL_{API} values decrease significantly to 13.6 mL and 8.4 mL, respectively. The nano-barrier effect of the SLS-MMT nanosheets protects the colloids from Na⁺ and thermal degradation. As shown in Fig. 15(a), FL_{API} increases as the temperature increases, and 0.5 wt% AAA/1.0 wt% SLS-MMT always exhibits the smallest FL_{API} of the saturated brine system, indicating that it is the best filtration-loss-reducing agent for the saturated brine system. Fig. 15(b) shows the FLAPI values in a composite brine system containing Na⁺, Ca²⁺, and Mg²⁺. Owing to the presence of additional

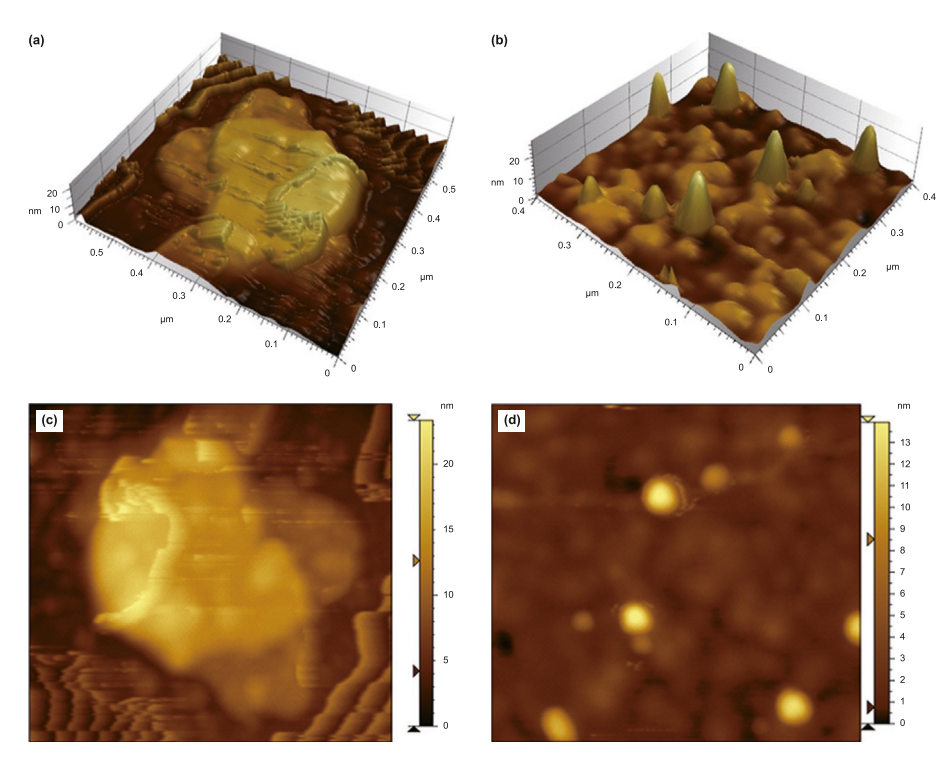


Fig. 10. AFM images of (a), (c) AAA and (b), (d) AAA/1.0 wt% SLS-MMT.

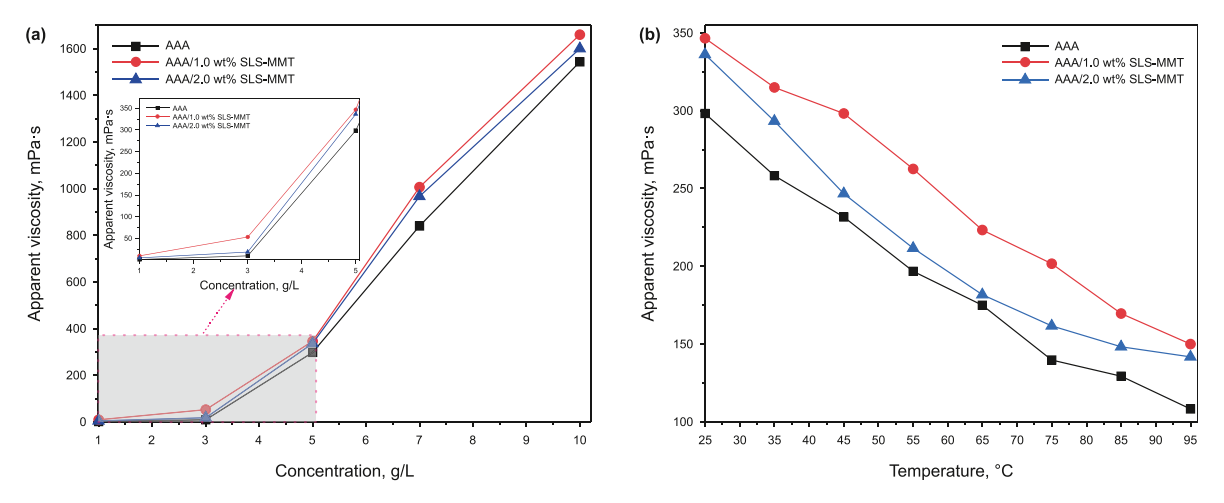


Fig. 11. AV plots of AAA, AAA/1.0 wt% SLS-MMT, and AAA/2.0 wt% SLS-MMT as functions of (a) concentration and (b) temperature.

Ca²⁺ and Mg²⁺, FL_{API} is further increased compared to that of the solution containing only Na⁺. FL_{API} for the composite brine system at 180 °C was 200 mL, while FL_{API} for brine systems containing 0.5 wt% AAA and 0.5 wt% AAA/1.0 wt% SLS-MMT was 84 and 80 mL, respectively. Compared with the saturated brine systems, the significantly higher FL_{API} values of the composite systems indicate that Ca²⁺ and Mg²⁺ cause more damage to the drilling fluid colloid. Therefore, ways to improve the filtration capacity of composite drilling fluid systems should necessarily be investigated in the future. In conclusion, all findings indicated that AAA/1.0 wt% SLS-MMT possesses the capacity to be applied in reservoirs with high salt and temperature as a fluid loss-reducing agent.

3.11.3. Surface morphology of the filtrate cakes

Filter cakes were obtained following a 16 h ageing process at a temperature of 220 °C in freshwater to further evaluate the

filtration performance. In Fig. 16(a), the filter cake devoid of 0.5 wt% AAA/1.0 wt% SLS-MMT is thick (4.86 mm) and inflexible and its surface is uneven, with holes and bumps. The SEM image confirms this surface morphology (Fig. 16(c)). The filtrate can pass freely through the tiny pores, resulting in a substantial filtration loss of 40.0 mL. The filter cake containing 0.5 wt% AAA/1.0 wt% SLS-MMT, on the other hand, possesses a smooth surface (Fig. 16(b) and (d)) and is thinner (0.81 mm) and more flexible (consistent with its reduced filtration loss of 11.8 mL) because of the high adsorption between the SLS-MMT layers and the polymer chains. Consequently, AAA/1.0 wt% SLS-MMT maintains uniformity and stability in WBDFs systems even at high temperatures.

3.12. Stability of fresh WBDFs system

An ideal drilling fluid colloid can improve the penetration rate

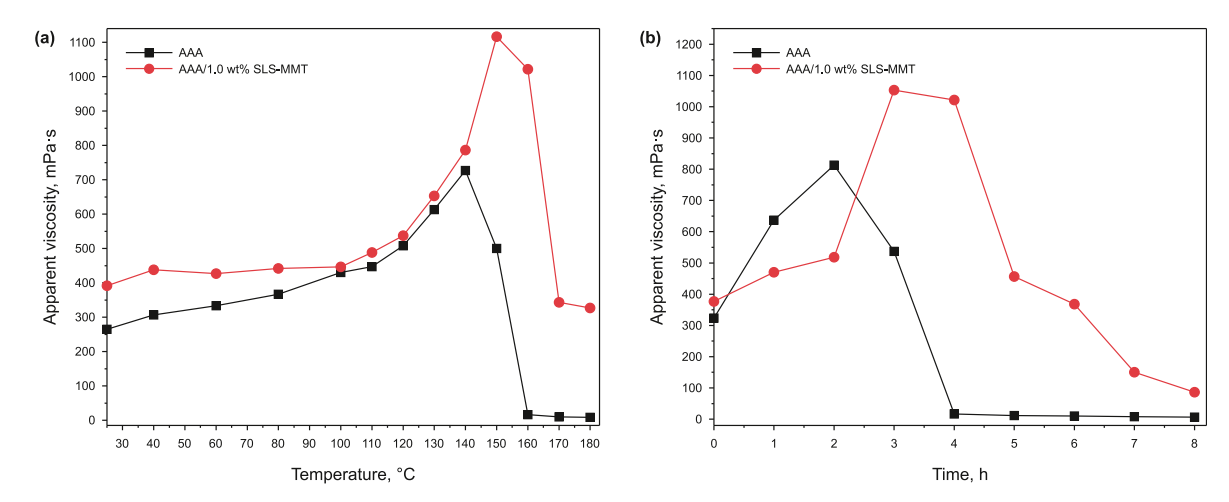


Fig. 12. AV plots of AAA, AAA/1.0 wt% SLS-MMT as a function of the (a) ageing temperature after 4 h and (b) ageing time at 160 °C.

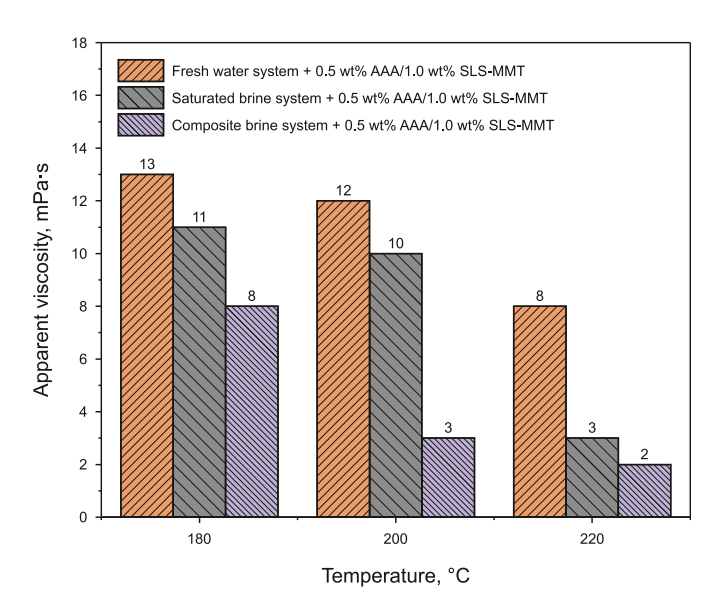


Fig. 13. AV of WBDFs with 0.5 wt% AAA/1.0 wt% SLS-MMT.

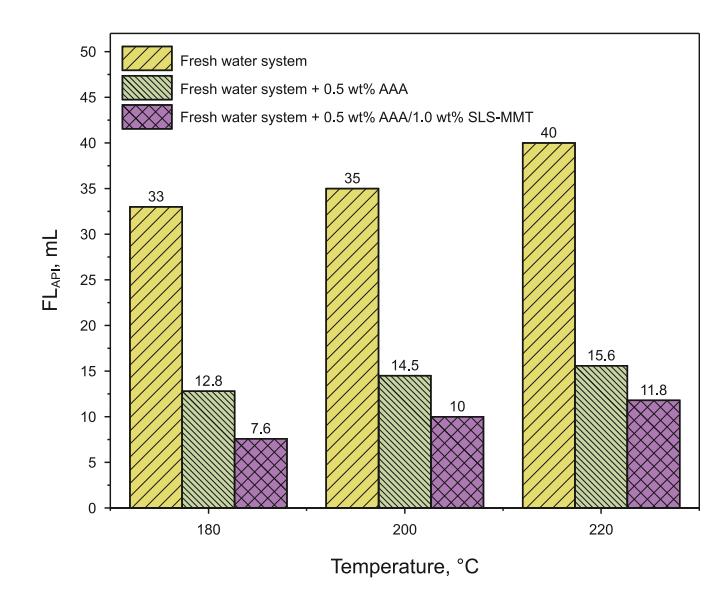


Fig. 14. FLAPI of fresh WBDFs systems.

and stabilize the wellbore during well drilling. Fig. 17 shows the 4.0 wt% freshwater-based simulated drilling fluid system left at room temperature for 60 days. In the absence of 0.5 wt% AAA/1.0 wt % SLS-MMT (Fig. 17(a)), the drilling fluid is unstable and significant sedimentation occurs. However, the drilling fluid with 0.5 wt% AAA/1.0 wt% SLS-MMT remains stable because the MMT nanosheets prevent the clay particles from bridging and agglomerating, thereby keeping them in solution (Fig. 17(b)). A greater absolute zeta potential typically signifies enhanced electrostatic repulsion among colloidal particles, thereby contributing to a more stable dispersion. Zeta potentials were determined for simulated freshwater-based drilling fluid systems containing 4.0 wt% MMT and 0 or 0.5 wt% AAA/1.0 wt% SLS-MMT. The system containing AAA/1.0 wt% SLS-MMT exhibited a greater absolute zeta potential (38.9 mV) in comparison to the control group (20.7 mV), displayed in Table 2. The silicate nanosheets can be effectively adsorbed by the functional groups present on AAA/1.0 wt% SLS-MMT, including N, O, -OH, -NH₂, and -SO₃H on six-membered rings. Therefore, as a consequence of the increased electrostatic repulsion among the clay particles, the colloid became more stable, leading to exceptional filtration performance.

3.13. Adsorption energy between exfoliated nanosheets and polymer chains

Materials Studio software was used to calculate the adsorption energy between the SLS-MMT nanosheets and polymer chains. First, a universal force field was selected. The model of the exfoliated MMT nanosheet was established based on the reports of Skipper et al. (1995) and Heinz et al. (2005). Subsequently, the polymer and adsorption models were established and optimized in sequence. According to the calculation, the total energy of the entire system is 27060.06 kcal/mol and the energies of the exfoliated MMT nanosheet and the polymer are 36243.72 kcal/mol and 3848.40 kcal/mol, respectively. According to Eq. (3), the energy between the exfoliated MMT nanosheets and polymer is -13032.06 kcal/mol. Oxygen-containing functional groups on the exfoliated monolayer can combine with amino (NH₂) and sulfonic acid (SO₃H) groups as well as the N and O atoms in the sixmembered ring of the polymer side chain to form hydrogen bonds (see Fig. 18). Strong interactions, such as intermolecular forces and van der Waals forces, also impart polymer nanocomposites with good high-temperature resistance. These calculations confirm the results of the SEM, AFM, XPS, TEM, and zeta potential investigations. The adsorption groups on the side chains

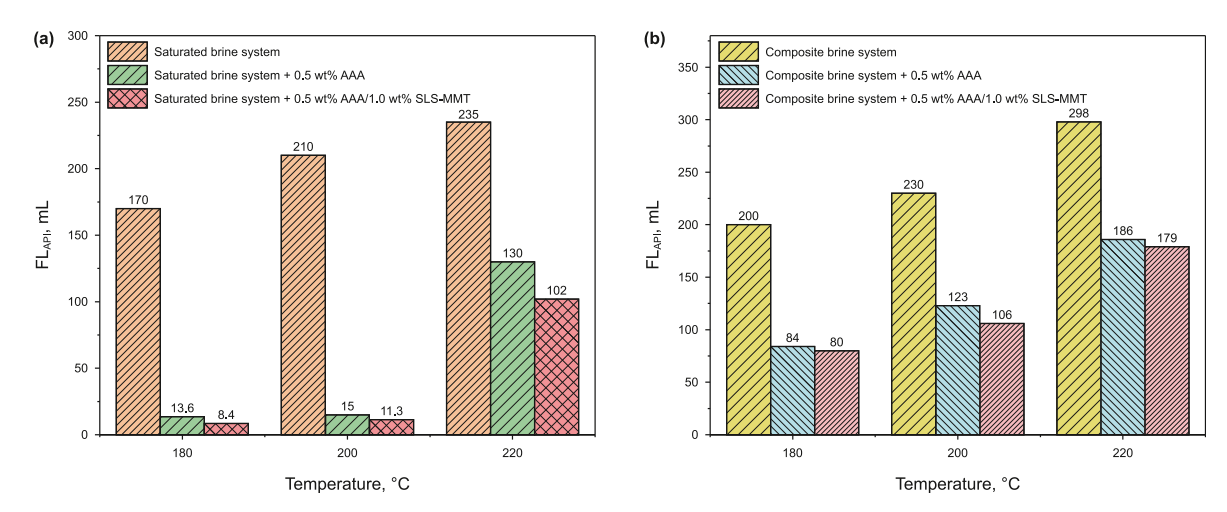


Fig. 15. FL_{API} of (a) saturated and (b) composite brine-based drilling fluid systems.

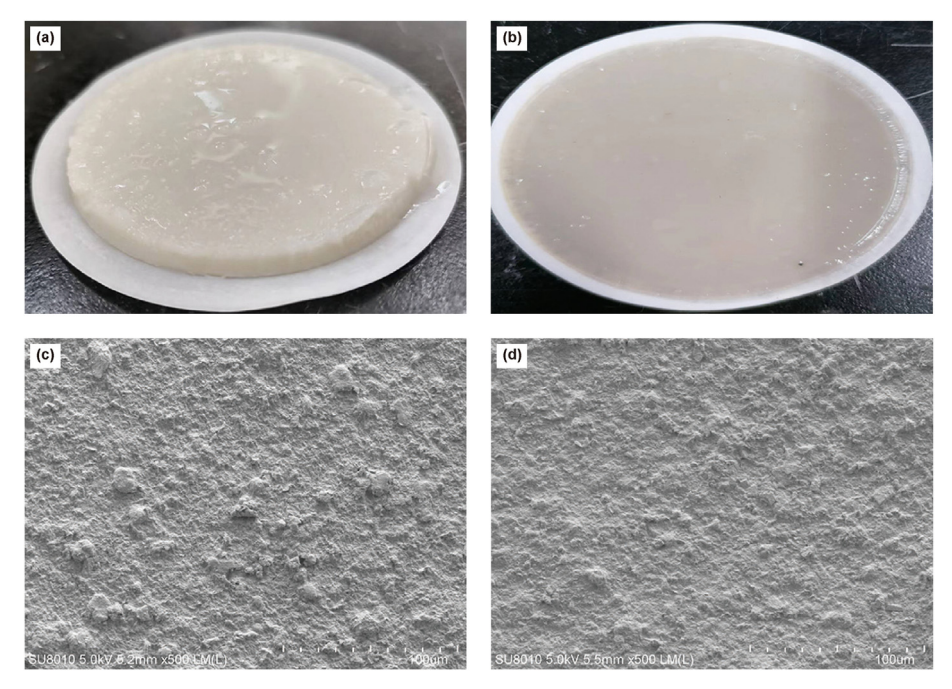


Fig. 16. (a), (b) Photographs and (c), (d) SEM images of the filter cakes. (a), (c) Without and (b), (d) with 0.5 wt% AAA/1.0 wt% SLS-MMT.





Fig. 17. Photographs of a simulated fresh WBDFs system **(a)** without and **(b)** with 0.5 wt% AAA/1.0 wt% SLS-MMT after being kept at room temperature for 60 days.

of polymer chains, such as NH₂, SO₃H, etc., strongly adsorb with the exfoliated SLS-MMT. The strong adsorption can promote to form a thick hydrated shell on the surface of clay particles in drilling fluid, inhibiting their dehydration at high-temperature. At the same time, this strong adsorption is able to restrain the desorption of clay particles on their surface in the drilling fluid (Greesh et al., 2008). In summary, exfoliated SLS-MMT nanosheets are strongly adsorbed on the polymer chain to form a high-temperature resistant polymer nanocomposite (AAA/SLS-MMT) with great potential as an additive for WBDFs.

4. Conclusions

A water-soluble high-temperature resistant polymer nano-composite (AAA/SLS-MMT) was synthesized by the free-radical in situ polymerization of AM, AMPS, ACMO, and SLS-MMT. XRD, FT-IR, and ¹H-NMR analyses verified the successful synthesis of AAA/SLS-

Table 2Zeta potentials of simulated drilling fluid systems (4.0 wt%) containing freshwater.

Addition amount of AAA/1.0 wt% SLS-MMT, wt%	Zeta potential, m	Zeta potential, mV				
	1st	2nd	3rd	Average		
0	-20.7	-21.3	-20.1	-20.7		
0.5	-39.6	-38.3	-38.9	-38.9		

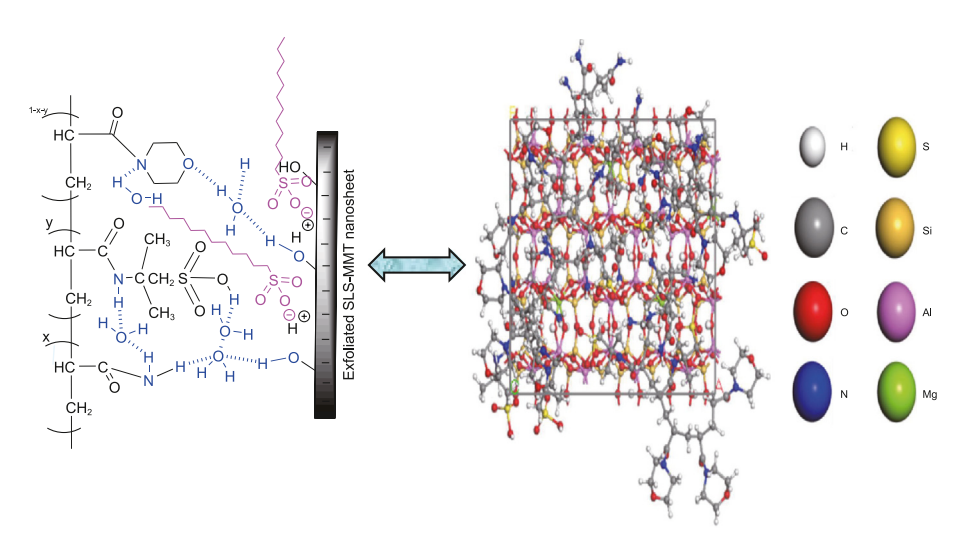


Fig. 18. Calculation model of adsorption energy between the exfoliated nanosheet of SLS-MMT and polymer chains.

MMT. SEM, TEM, and AFM were employed to observe the strongly adsorbed exfoliated SLS-MMT nanosheets on the polymer chains. XPS, colloidal stability, and zeta potential experiments also confirmed the strong adsorption between the polymer and the exfoliated nanosheets. Moreover, molecular simulation software was employed to determine the adsorption energy between the polymer chain and the exfoliated nanosheets. Ageing and filtration reduction experiments showed that AAA/1.0 wt% SLS-MMT notably enhanced the resistance of WBDFs to elevated temperatures. The strong adsorption was able to inhibit the dehydration and the desorption of clay particles in drilling fluid at high temperatures. Also, the exfoliated nanosheets demonstrated substantial adsorption on the polymer chains' surface and functioned as nanobarriers to prevent the degradation of the polymer in high-temperature and high-Na⁺ conditions. However, in the presence of Ca²⁺ and Mg²⁺, the reduction in filtration loss was poor, which requires further study. In conclusion, AAA/1.0 wt% SLS-MMT is a promising filtrateloss-reducing additive for WBDFs in high-temperature and highsalt reservoirs.

CRediT authorship contribution statement

Dong-Yin Wang: Writing — original draft, Investigation. **Chang-Feng Chen:** Validation, Investigation, Data curation. **Fei Ju:** Formal analysis. **Yang-Chuan Ke:** Writing — review & editing, Supervision, Methodology.

Declaration of competing interest

The authors declare that they have no known competing financial interests or personal relationships that could have appeared to influence the work reported in this paper.

Acknowledgements

This work was financially supported by the National Major Project (No. 2017ZX05009-003,50), National Natural Science Foundation of China (No. 51974339; 51674270), Foreign Expert Project of the Belt and Road Innovation Talents Exchange (DL2022122001), and the Research Institute of Petroleum Exploration Development of China National Petroleum Cooperation (HX20201095).

References

Abdel Karim, A., El Naggar, M.E., Radwan, E.K., et al., 2021. High-performance mixed-matrix membranes enabled by organically/inorganic modified montmorillonite for the treatment of hazardous textile wastewater. Chem. Eng. J. 405, 126964. https://doi.org/10.1016/j.cej.2020.126964.

Abdo, J., Haneef, M.D., 2013. Clay nanoparticles modified drilling fluids for drilling of deep hydrocarbon wells. Appl. Clay Sci. 86, 76–82. https://doi.org/10.1016/ j.clay.2013.10.017.

Aghdam, S.B., Moslemizadeh, A., Kowsari, E., et al., 2020. Synthesis and performance evaluation of a novel polymeric fluid loss controller in water-based drilling fluids: high-temperature and high-salinity conditions. J. Nat. Gas Sci. Eng. 83, 103576. https://doi.org/10.1016/j.jngse.2020.103576.

Akhtarmanesh, S., Shahrabi, M.J.A., Atashnezhad, A., 2013. Improvement of wellbore stability in shale using nanoparticles. J. Petrol. Sci. Eng. 112, 290–295. https://doi.org/10.1016/j.petrol.2013.11.017.

Akpan, E.Ü., Enyi, G.C., Nasr, G., et al., 2019. Water-based drilling fluids for high-temperature applications and water-sensitive and dispersible shale formations. J. Petrol. Sci. Eng. 175, 1028–1038. https://doi.org/10.1016/j.petrol.2019.01.002.

Alani, S., Hassan, M.S., Jaber, A.A., et al., 2020. Effects of elevated temperatures on strength and microstructure of mortar containing nano-calcined montmorillonite clay. Construct. Build. Mater. 263, 120895. https://doi.org/10.1016/ j.conbuildmat.2020.120895.

Baba Hamed, S., Belhadri, M., 2009. Rheological properties of biopolymers drilling fluids. J. Petrol. Sci. Eng. 67 (3–4), 84–90. https://doi.org/10.1016/ j.petrol.2009.04.001.

Bensalem, S., Hamdi, B., Del Confetto, S., et al., 2017. Characterization of chitosan/ montmorillonite bionanocomposites by inverse gas chromatography. Colloids Surf. A Physicochem. Eng. Asp. 516, 336–344. https://doi.org/10.1016/ i.colsurfa.2016.12.051.

Briesenick, D., Bremser, W., 2015. Synthesis of polyamide-imide-montmorillonite-

nanocomposites via new approach of in situ polymerization and solvent casting. Prog. Org. Coating 82, 26—32. https://doi.org/10.1016/j.porgcoat.2015.01.013.

- Chaudhary, D., Liu, H., 2013. Ultrasonic treatment and synthesis of sugar alcohol modified Na⁺-montmorillonite clay. Ultrason. Sonochem. 20 (1), 63–68. https://doi.org/10.1016/j.ultsonch.2012.08.003.
- Chen, M.S., Fu, W.W., Hu, Y.J., et al., 2020. Controllable growth of carbon nanosheets in the montmorillonite interlayers for high-rate and stable anode in lithium ion battery. Nanoscale 12 (30), 16262–16269. https://doi.org/10.1039/d0nr03962d.
- Chen, T.X., Yuan, Y., Zhao, Y.L., et al., 2019. Preparation of montmorillonite nanosheets through freezing/thawing and ultrasonic exfoliation. Langmuir 35 (6), 2368–2374. https://doi.org/10.1021/acs.langmuir.8b04171.
- Chin, I.-J., Thurn-Albrecht, T., Kim, H.-C., et al., 2001. On exfoliation of montmorillonite in epoxy. Polymer 42 (42), 5947–5952. https://doi.org/10.1016/S0032-3861(00)00898-3.
- Chiou, J.Y., Huang, T.K., Hsieh, K.H., et al., 2014. Fine dispersion of phosphazeneamines and silicate platelets in epoxy nanocomposites and the synergistic fire-retarding effect. J. Polym. Res. 21 (6), 467. https://doi.org/10.1007/s10965-014-0467-7.
- Coleman, J.N., Lotya, M., O'Neill, A., et al., 2011. Two-dimensional nanosheets produced by liquid exfoliation of layered materials. Science 331 (6017), 568–571. https://doi.org/10.1126/science.1194975.
- Dziadkowiec, J., Mansa, R., Quintela, A., et al., 2017. Preparation, characterization and application in controlled release of ibuprofen-loaded guar gum/montmo-rillonite bionanocomposites. Appl. Clay Sci. 135, 52–63. https://doi.org/10.1016/i.clay.2016.09.003.
- Ejder Korucu, M., Gürses, A., Karaca, S., 2016. Poly(ethylene oxide)/clay nanaocomposites: thermal and mechanical properties. Appl. Surf. Sci. 378, 1–7. https://doi.org/10.1016/j.apsusc.2016.03.159.
- Epelle, E.I., Gerogiorgis, D.I., 2019. A review of technological advances and open challenges for oil and gas drilling systems engineering. AIChE J. 66 (4), 16842. https://doi.org/10.1002/aic.16842.
- Fekry, M., Mazrouaa, A.M., Mohamed, M.G., et al., 2020. Properties of polyethylcyanoacrylate/modified Mt composites with highly exfoliated montmorillonite. Polym. Bull. 78 (10), 5685–5711. https://doi.org/10.1007/s00289-020-03402-1.
- Galimberti, M., Coombs, M., Cipolletti, V., et al., 2014. Delaminated and intercalated organically modified montmorillonite in poly(1,4-cis-isoprene) matrix. Indications of counterintuitive dynamic-mechanical behavior. Appl. Clay Sci. 97, 8–16. https://doi.org/10.1016/j.clay.2014.05.010.
- Greesh, N., Hartmann, P.C., Cloete, V., et al., 2008. Adsorption of 2-acrylamido-2-methyl-1-propanesulfonic acid (AMPS) and related compounds onto montmorillonite clay. J. Colloid Interface Sci. 319 (1), 2—11. https://doi.org/10.1016/j.jcis.2007.10.019.
- Gunning, M.A., Geever, L.M., Killion, J.A., et al., 2014. The effect of the mixing routes of biodegradable polylactic acid and polyhydroxybutyrate nanocomposites and compatibilised nanocomposites. J. Thermoplast. Compos. Mater. 29 (4), 538–557. https://doi.org/10.1177/0892705714526912.
- Hafshejani, K.S., Moslemizadeh, A., Shahbazi, K., 2016. A novel bio-based deflocculant for bentonite drilling mud. Appl. Clay Sci. 127, 23–34. https://doi.org/ 10.1016/j.clay.2016.03.037.
- Hao, S.Q., 2019. Development of portable drilling fluid and seepage simulation for deep saline aquifers. J. Petrol. Sci. Eng. 175, 560–572. https://doi.org/10.1016/ j.petrol.2018.12.070.
- Heinz, H., Koerner, H., Anderson, K.L., et al., 2005. Force field for mica-type silicates and dynamics of octadecylammonium chains grafted to montmorillonite. Chem. Mater. 17, 5658–5669. https://doi.org/10.1021/cm0509328.
- Hojiyev, R., Ulcay, Y., Çelik, M.S., et al., 2017. Effect of CEC coverage of hexadecyl-tributylphosphonium modified montmorillonite on polymer compatibility. Appl. Clay Sci. 141, 204–211. https://doi.org/10.1016/j.clay.2017.02.036.
- Hu, X., Ke, Y.C., 2019. The influence of organic modified montmorillonite on the solution properties of copolymer containing β-cyclodextrin. J. Polym. Res. 27 (1), 19. https://doi.org/10.1007/s10965-019-1990-3.
- Huang, T.K., Chiou, J.Y., Wang, Y.C., et al., 2016. Unusual exfoliation of layered silicate clays by non-aqueous amine diffusion mechanism. J. Polym. Res. 23 (8), 151. https://doi.org/10.1007/s10965-016-1035-0.
- Huang, W.J., Liu, J.H., She, Q.M., et al., 2021. Recent advances in engineering montmorillonite into catalysts and related catalysis. Catal. Rev. 1 (1), 1–57. https://doi.org/10.1080/01614940.2021.1995163.
- Huo, J.H., Peng, Z.G., Ye, Z.B., et al., 2018. Investigation of synthesized polymer on the rheological and filtration performance of water-based drilling fluid system. J. Petrol. Sci. Eng. 165, 655–663. https://doi.org/10.1016/j.petrol.2018.03.003.
- Ke, Y.C., 2009. Polymer Nanocomposites, first ed. Science Press, Beijing (in Chinese).
- Li, H., Huang, X.B., Sun, J.S., et al., 2023. Improving the anti-collapse performance of water-based drilling fluids of Xinjiang Oilfield using hydrophobically modified silica nanoparticles with cationic surfactants. Petrol. Sci. 20 (3), 1768–1778. https://doi.org/10.1016/j.petsci.2022.10.023.
- Li, L.L., Zhang, X.H., Wang, Y.L., et al., 2016. Simulation of mechanical properties based on microstructure in polyethylene/montmorillonite nanocomposites. Acta Phys. Sin. 65 (19), 196202. https://doi.org/10.7498/aps.65.196202.
- Liu, J.P., Dai, Z.W., Xu, K., et al., 2020. Water-based drilling fluid containing bentonite/poly(sodium 4-styrenesulfonate) composite for ultrahightemperature ultradeep drilling and its field performance. SPE J. 25 (3), 1193–1203. https://doi.org/10.2118/199362-pa.
- Liu, L., Pu, X., Tao, H., et al., 2018. Synthesis and characterization of comb-shaped

copolymer as a filtration reducer and comparison with counterparts. RSC Adv. 8 (21), 11424–11435. https://doi.org/10.1039/c7ra13255g.

- Luckham, P.F., Rossi, S., 1999. The colloidal and rheological properties of bentonite suspensions. Adv. Colloid Interface Sci. 82, 43–92. https://doi.org/10.1007/ s10965-016-1035-0
- Luo, Z.H., Wang, L.X., Pei, J.J., et al., 2018. A novel star-shaped copolymer as a rheology modifier in water-based drilling fluids. J. Petrol. Sci. Eng. 168, 98–106. https://doi.org/10.1016/j.petrol.2018.05.003.
- Ma, J., An, Y., Yu, P., 2018. Core—shell structure acrylamide copolymer grafted on nano-silica surface as an anti-calcium and anti-temperature fluid loss agent. I. Mater. Sci. 54 (7), 5927—5941. https://doi.org/10.1007/s10853-018-03239-0.
- Ma, R., Sasaki, T., 2010. Nanosheets of oxides and hydroxides: Ultimate 2D charge-bearing functional crystallites. Adv. Mater. 22 (45), 5082–5104. https://doi.org/10.1002/adma.201001722.
- Mohamed, A., Salehi, S., Ahmed, R., 2021. Significance and complications of drilling fluid rheology in geothermal drilling: a review. Geothermics 93, 102066. https://doi.org/10.1016/j.geothermics.2021.102066.
- Moslemizadeh, A., Khezerloo ye Aghdam, S., Shahbazi, K., et al., 2017. A triterpenoid saponin as an environmental friendly and biodegradable clay swelling inhibitor. J. Mol. Liq. 247, 269–280. https://doi.org/10.1016/j.molliq.2017.10.003.
- Osman, A.F., Alakrach, A.M., Kalo, H., et al., 2015. In vitro biostability and biocompatibility of ethyl vinyl acetate (EVA) nanocomposites for biomedical applications. RSC Adv. 5 (40), 31485–31495. https://doi.org/10.1039/c4ra15116j.
- Peng, J., Tomsia, A.P., Jiang, L., et al., 2021. Stiff and tough PDMS-MMT layered nanocomposites visualized by AIE luminogens. Nat. Commun. 12 (1), 4539. https://doi.org/10.1038/s41467-021-24835-w.
- Quainoo, A.K., Negash, B.M., Bavoh, C.B., et al., 2021. Natural amino acids as potential swelling and dispersion inhibitors for montmorillonite-rich shale formations. J. Petrol. Sci. Eng. 196, 107664. https://doi.org/10.1016/j.petrol.2020.107664.
- Roghani Mamaqani, H., Haddadi Asl, V., Najafi, M., et al., 2011. Preparation of nanoclay-dispersed polystyrene nanofibers via atom transfer radical polymerization and electrospinning. J. Appl. Polym. Sci. 120 (3), 1431–1438. https://doi.org/10.1002/app.33119.
- Saboori, R., Sabbaghi, S., Kalantariasl, A., 2019. Improvement of rheological, filtration and thermal conductivity of bentonite drilling fluid using copper oxide/polyacrylamide nanocomposite. Powder Technol. 353, 257–266. https://doi.org/10.1016/j.powtec.2019.05.038.
- Sepehri, S., Soleyman, R., Varamesh, A., et al., 2018. Effect of synthetic water-soluble polymers on the properties of the heavy water-based drilling fluid at high pressure-high temperature (HPHT) conditions. J. Petrol. Sci. Eng. 166, 850–856. https://doi.org/10.1016/j.petrol.2018.03.055.
- Skipper, N.T., Boek, E.S., Coveney, P.V., 1995. Molecular modeling of clay hydration: a study of hysteresis loops in the swelling curves of sodium montmorillonites. Langmuir 11, 4629–4631. https://doi.org/10.1021/la00012a008.
- Slaný, M., Jankovič, L., Madejová, J., 2019. Structural characterization of organomontmorillonites prepared from a series of primary alkylamines salts: Mid-IR and near-IR study. Appl. Clay Sci. 176, 11–20. https://doi.org/10.1016/ j.clay.2019.04.016.
- Tian, Y., Wu, Y., Wang, Z., et al., 2019. Fe₃O₄/poly (acrylic acid) nanoparticles as modifiers for improving rheological and filtration properties of water-based drilling fluids. J. Macromol. Sci., Part A 56 (5), 393–402. https://doi.org/10.1080/10601325.2019.1578619.
- Wang, D.Y., Chen, C.F., Ju, F., et al., 2022a. Copolymer nanocomposites with strong adsorption of exfoliated silicate nanosheets and high-temperature stability. New J. Chem. 46, 21672–21683. https://doi.org/10.1039/D2NJ03925G.
- Wang, D.Y., Chen, C.F., Hu, X.J., et al., 2023. Enhancing the properties of water-soluble copolymer nanocomposites by controlling the layer silicate load and exfoliated nanolayers adsorbed on polymer chains. Polymers 15, 1413. https://doi.org/10.3390/polym15061413.
- Wang, F., Fu, H.F., Wang, F.X., et al., 2022b. Enhanced catalytic sulfamethoxazole degradation via peroxymonosulfate activation over amorphous CoSx@SiO₂ nanocages derived from ZIF-67. J. Hazard Mater. 423, 126998. https://doi.org/ 10.1016/j.jhazmat.2021.126998.
- Wang, F.H., Tan, X.C., Wang, R.H., et al., 2012. High temperature and high pressure rheological properties of high-density water-based drilling fluids for deep wells. Petrol. Sci. 9 (3), 354–362. https://doi.org/10.1007/s12182-012-0219-4.
- Weng, Z., Wang, J., Senthil, T., et al., 2016. Mechanical and thermal properties of ABS/montmorillonite nanocomposites for fused deposition modeling 3D printing. Mater. Des. 102, 276–283. https://doi.org/10.1016/j.matdes.2016.04.045.
- Xie, G., Huang, D., Xiao, Y., et al., 2020. Intercalation inhibits the surface hydration of sodium montmorillonite: experiments and density functional theory simulation. ACS Sustain. Chem. Eng. 8 (27), 10303–10312. https://doi.org/10.1021/ acssuschemeng.0c03943.
- Xing, L., Ke, Y.C., Hu, X., et al., 2020. Preparation and solution properties of polyacrylamide-based silica nanocomposites for drag reduction application. New J. Chem. 44 (23), 9802–9812. https://doi.org/10.1039/c9nj05583e.
- Xing, L., Ke, Y.C., Hu, X., et al., 2019. Preparation and properties of amphoteric polyacrylamide/modified montmorillonite nanocomposites and its drag reduction performance. Colloids Surf. A Physicochem. Eng. Asp. 574, 94–104. https://doi.org/10.1016/j.colsurfa.2019.04.078.
- Yang, F., Mubarak, C., Keiegel, R., et al., 2017a. Supercritical carbon dioxide (scCO₂) dispersion of poly(ethylene terephthalate)/clay nanocomposites: structural, mechanical, thermal, and barrier properties. J. Appl. Polym. Sci. 134 (18), 44779.

https://doi.org/10.1002/app.44779.

- Yang, L.L., Jiang, G.C., Shi, Y.W., et al., 2017b. Application of ionic liquid to a high-performance calcium-resistant additive for filtration control of bentonite/water-based drilling fluids. J. Mater. Sci. 52 (11), 6362–6375. https://doi.org/10.1007/s10853-017-0870-7.
- Yu, C.C., Ke, Y.C., Hu, X., et al., 2019. Effect of bifunctional montmorillonite on the thermal and tribological properties of polystyrene/montmorillonite nanocomposites. Polymers 11 (5), 834. https://doi.org/10.3390/polym11050834.
- Yu, P.Z., 2015. Modification of waste polyacrylonitrile fiber and its application as a filtrate reducer for drilling. Petrol. Sci. 12 (2), 325–329. https://doi.org/10.1007/s12182-015-0019-8.
- Zhang, G.L., Ke, Y.C., He, J., et al., 2015. Effects of organo-modified montmorillonite on the tribology performance of bismaleimide-based nanocomposites. Mater. Des. 86, 138–145. https://doi.org/10.1016/j.matdes.2015.07.090.
- Zhang, S., Zhang, Z., Li, B., et al., 2021. Hierarchical Ag₃PO₄@ZnIn₂S₄ nanoscoparium:

- an innovative Z-scheme photocatalyst for highly efficient and predictable tetracycline degradation. J. Colloid Interface Sci. 586, 708–718. https://doi.org/10.1016/j.jcis.2020.10.140.
- Zhao, M.Z., Wu, H.M., Zhu, Z., et al., 2022. Preparation of polyethylene nano-composites based on polyethylene grafted exfoliated α-zirconium phosphate. Macromolecules 55 (8), 3039–3050. https://doi.org/10.1021/acs.macromol.2c00038.
- Zhao, Y., Kang, S., Qin, L., et al., 2020. Self-assembled gels of Fe-chitosan/montmorillonite nanosheets: dye degradation by the synergistic effect of adsorption and photo-Fenton reaction. Chem. Eng. J. 379, 122322. https://doi.org/10.1016/j.cej.2019.122322.
- Zhu, T.T., Zhou, C.H., Kabwe, F.B., et al., 2019. Exfoliation of montmorillonite and related properties of clay/polymer nanocomposites. Appl. Clay Sci. 169, 48–66. https://doi.org/10.1016/j.clay.2018.12.006.